nature communications

Article

https://doi.org/10.1038/s41467-026-69452-7

Perfectly harmonic spin cycloid and multi-Q textures in the Weyl semimetal GdAlSi

Received: 27 March 2025

Accepted: 2 February 2026

Published online: 23 February 2026

Check for updates

Ryota Nakano[1], Rinsuke Yamada[1] ✉, Juba Bouaziz[2] ✉, Maurice Colling[3,14], Masaki Gen[4,5], Kentaro Shoriki[1], Yoshihiro Okamura[1], Akiko Kikkawa[4], Ryo Misawa[1], Priya R. Baral[1], Shunsuke Kitou[6], Yuiga Nakamura[7], Hiroyuki Ohsumi[8], Yoshikazu Tanaka[8], Hajime Sagayama[9], Hironori Nakao[9], Yuki Ishihara[1], Kamini Gautam[4], Oscar Fabelo[10], Yasujiro Taguchi[4], Youtarou Takahashi[1,4], Masashi Tokunaga[4,5], Taka-hisa Arima[4,6], Yoshinori Tokura[1,4,11], Ryotaro Arita[4,12], Jan Masell[3,4], Satoru Hayami[13] & Max Hirschberger[1,4] ✉

A fundamental question in condensed matter physics concerns how topological electronic states are influenced by many-body correlations, and magnetic Weyl semimetals represent an important material platform to address this problem. However, the magnetic structures realized in these materials are limited, and in particular, no clear example of an undistorted helimagnetic state has been definitively identified. Here, we report clear evidence of a harmonic helimagnetic cycloid with an incommensurate magnetic propagation vector **Q** in the Weyl semimetal GdAlSi via resonant elastic X-ray scattering, including rigorous polarization analysis. This cycloidal structure is consistent with the Dzyaloshinskii–Moriya interaction prescribed by the polar crystal structure of GdAlSi. Upon applying a magnetic field, the cycloid undergoes a transition to a novel multi-**Q** state. This field-induced, noncoplanar texture is consistent with our numerical spin model, which incorporates the Dzyaloshinskii–Moriya interaction and, crucially, anisotropic exchange interactions. The perfectly harmonic Weyl helimagnet GdAlSi serves as a prototypical platform to study electronic correlation effects in periodically modulated Weyl semimetals.

Inversion-breaking Weyl semimetals host two-fold degenerate band crossings with a quasi-relativistic, linear energy-momentum dispersion and protected surface Fermi arcs[1]. As such, inversion breaking Weyl semimetals provide a platform to study the interplay between many-body correlations and topologically nontrivial electronic states. Relevant proposals include the formation of an axion insulator[2–4] and a three-dimensional fractional quantum Hall effect from disordered domains in a Weyl charge-density-wave[5–7]. Such states are realized by

[1]Department of Applied Physics and Quantum-Phase Electronics Center, The University of Tokyo, Tokyo, Japan. [2]Research Center for Advanced Science and Technology, The University of Tokyo, Tokyo, Japan. [3]Institute of Theoretical Solid State Physics, Karlsruhe Institute of Technology (KIT), Karlsruhe, Germany. [4]RIKEN Center for Emergent Matter Science (CEMS), Wako, Saitama, Japan. [5]Institute for Solid State Physics, The University of Tokyo, Kashiwa, Japan. [6]Department of Advanced Materials Science, The University of Tokyo, Kashiwa, Japan. [7]Japan Synchrotron Radiation Research Institute (JASRI), Hyogo, Japan. [8]RIKEN SPring-8 Center, Hyogo, Japan. [9]Institute of Materials Structure Science, High Energy Accelerator Research Organization, Tsukuba, Ibaraki, Japan. [10]Institut Laue-Langevin, Grenoble, France. [11]Tokyo College, The University of Tokyo, Tokyo, Japan. [12]Department of Physics, The University of Tokyo, Tokyo, Japan. [13]Graduate School of Science, Hokkaido University, Sapporo, Japan. [14]Present address: Department of Materials Science and Engineering, Norwegian University of Science and Technology (NTNU), Trondheim, Norway. ✉e-mail: ryamada@ap.t.u-tokyo.ac.jp; jbouaziz@g.ecc.u-tokyo.ac.jp; hirschberger@ap.t.u-tokyo.ac.jp

band-folding of Weyl fermions into a small Brillouin zone upon formation of periodically modulated order, and conditions for the hybridization of Weyl points have been derived and phrased in the language of special relativity[8]. In this context, topics of interest have been not only charge order but also the formation of periodically modulated helimagnetic states in inversion broken Weyl semimetals, and the question of the relevant magnetic interactions in such Weyl semimetals[9–15]. However, an ideal platform for studying the interplay of Weyl fermions with helimagnetism—a perfect and undistorted helimagnetic structure in an inversion breaking Weyl semimetal—has never been reported by quantitative polarization analysis in diffraction experiments[16,17].

Here, we report the undistorted, cycloidal helimagnetic ground state of GdAlSi with perfectly isotropic Gd^{3+}, a material in which Fermi arcs from Weyl nodes have been identified, and a possibly related anomalous Hall effect has been observed under a magnetic field; the experiment supersedes a prior numerical prediction of collinear antiferromagnetism (altermagnetism) in this material[18,19]. We further demonstrate a field-induced transition to a complex staggered cone structure, which represents a superposition of two magnetic waves, i.e., a multi-**Q** state. Our numerical spin calculations successfully reproduce the ground state and field-induced phase transitions of GdAlSi, emphasizing the role of symmetry-allowed Dzyaloshinskii-Moriya (DM) and anisotropic exchange interactions.

Results

Electronic and magnetic state of GdAlSi

GdAlSi crystallizes in the polar tetragonal $I4_1md$ structure with neither inversion center nor $\mathcal{M}_z$ mirror plane, leading to a Weyl semimetallic state that is strongly coupled to the magnetic texture, see Fig. 1a, b and Supplementary Fig. S4[12–14,18–26]. In this material class, ferromagnetism, canted ferromagnetism, topological antimerons, nearly collinear up-up-down order, and helimagnetic order have been reported from experiments on PrAlSi/Ge[27], CeAlSi[28], CeAlGe[29], NdAlSi/Ge[12,14,30], and SmAlSi[13], respectively. However, there is no prior confirmation of an undistorted helimagnetic order by polarization analysis, hindering discussion of the relevant exchange interactions. Figure 1a illustrates a subset of these electronic Weyl points in the electronic structure of noncentrosymmetric GdAlSi, and their approximate position close to the $k_c = 0$ plane of the tetragonal Brillouin zone in the paramagnetic state of noncentrosymmetric GdAlSi. In this article, we demonstrate the helimagnetic order in GdAlSi, which interconnects the Weyl points as indicated by yellow arrows in Fig. 1a, and which has the character of a harmonic cycloid defined by

$$\mathbf{m}(\mathbf{r}) = m(\mathbf{Q})\left[\mathbf{e}_{[110]}\cos(\mathbf{Q}\cdot\mathbf{r}) + \mathbf{e}_c\sin(\mathbf{Q}\cdot\mathbf{r})\right] \quad (1)$$

Here, $\mathbf{e}_{[110]}$ and $\mathbf{e}_c$ are unit vectors along the crystallographic [110]- and c-axes, respectively; $\mathbf{Q} = (q, q, 0)$ with $q = 0.673(2)$ reciprocal lattice units (r.l.u.) is a lattice-incommensurate propagation vector. This cycloidal spin texture and the corresponding magnetic unit cell are illustrated in Fig. 1b, where the staggered square lattices of gadolinium ions in GdAlSi are projected onto a single plane. The conventional unit cell of the magnetic state is about six times larger than the conventional unit cell of the paramagnetic state; primitive unit cells are discussed in Supplementary Fig. S9.

The period and propagation direction of the helimagnetic "wave" in GdAlSi are readily understood from the viewpoint of a minimal exchange Hamiltonian with isotropic nearest-neighbor interaction $J_1 < 0$ and inter-layer coupling $J_c < 0$, illustrated in Fig. 1c. Consistent

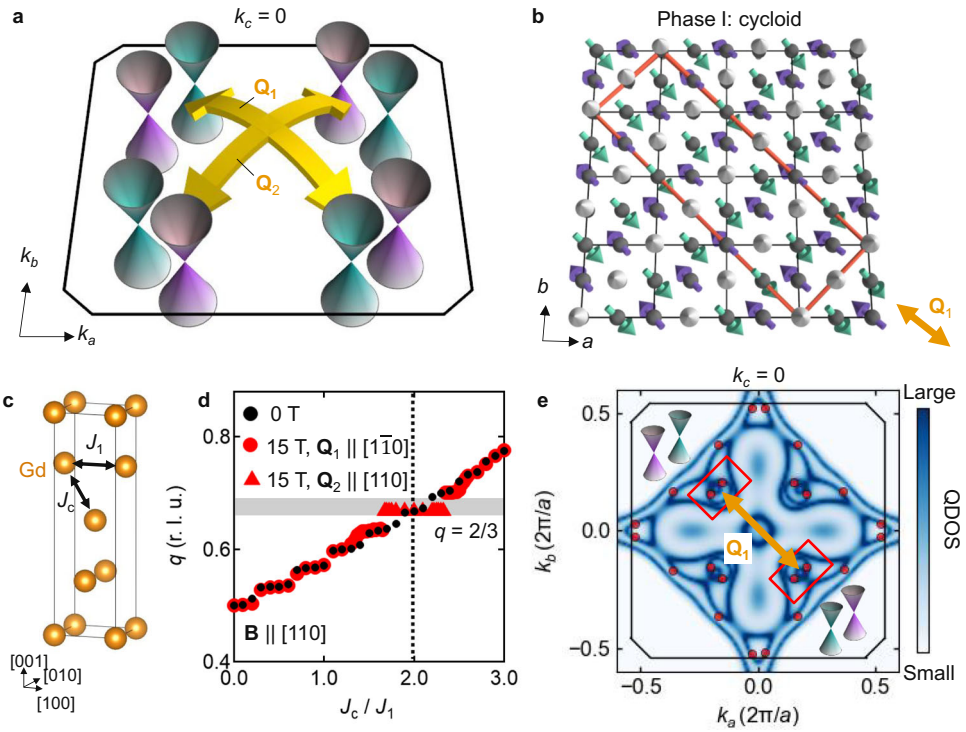

Fig. 1 | Undistorted helimagnetism in the Weyl semimetal GdAlSi. a Illustration of magnetic modulation vectors $\mathbf{Q}_1$, $\mathbf{Q}_2$ connecting between Weyl nodes in the electronic structure of GdAlSi. The black box indicates the $k_c = 0$ cut of the tetragonal Brillouin zone (BZ) in the paramagnetic state. **b** Experimentally observed cycloidal helimagnetic structure in the ground state of GdAlSi ($B = 0$) projected onto the (001) plane. Only magnetic Gd sites are shown; the black (red) boxes indicate a single unit cell in the paramagnetic (in the helimagnetic) state. **c** Gadolinium sublattice in the $I4_1md$ tetragonal structure of GdAlSi with definitions for nearest-neighbor (J_1) and next-nearest neighbor interactions (J_c). **d** Evolution of magnetic modulation vector $\mathbf{Q}_1 = (q, -q, 0)$ and $\mathbf{Q}_2 = (q, q, 0)$ for $J_1, J_c < 0$. A helimagnetic structure with $q = 2/3$ can be realized in this simple framework. **e** Calculated, momentum-resolved density of states (QDOS) in the $k_c = 0$ plane of the tetragonal BZ. 24 Weyl nodes (red circles) are found close to $k_c = 0$.

with the experiment, this natural choice of interactions (i) selects only propagation vectors of the type $\mathbf{Q}_{1,2} = (\pm q, \pm q, 0)$, constrained by tetragonal symmetry and (ii) reproduces the experimentally relevant range of q for a reasonable J_c/J_1 ratio (see Fig. 1d). Details of the calculation are given in Supplementary Note S5.

Importantly, the **Q**-vector observed experimentally in GdAlSi is well matched to the distance between sets of Weyl points in the electronic structure, as shown in our calculations of Fig. 1e. Prior work on NdAlSi has demonstrated a modification of quantum oscillations at the Weyl nodes below the onset of magnetic order[12]. The reciprocal effect of relativistic fermions on the magnetic structure, a strong contribution to magnetic interactions by Weyl electrons via modified Ruderman-Kittel-Kasuya-Yosida interactions, has not yet been conclusively demonstrated[9–11]. Indeed, electronic structure calculations on *R*AlSi (*R* = rare earth) show that states far from the Fermi energy predominantly fix the value of **Q**[31]. Therefore, Weyl nodes and helimagnetic order both exist in GdAlSi, but helimagnetism is not predominantly caused by the Weyl electrons and the matching of **Q** to the separation of Weyl points in momentum space is accidental, see also Supplementary Note S4.

Zero-field cycloid from resonant elastic X-ray scattering (REXS)

From magnetic susceptibility measurements and the resistivity ρ_{xx} in GdAlSi, we demonstrate a conducting ground state with a magnetic Néel point $T_N = 32$ K (Fig. 2a, b). The magnetic susceptibility has very weak anisotropy both above and below T_N (see Supplementary Fig. S3); ρ_{xx} appears affected by magnetic fluctuations above and around T_N, but fluctuations freeze out upon cooling. We employ resonant elastic X-ray scattering (REXS) measurements to reveal the helimagnetic order of GdAlSi (Methods). Figure 2c illustrates the experimental geometry of the sample with respect to the X-ray beam. Satellite magnetic peaks for two magnetic domains D1, D2 in vicinity of the fundamental Bragg reflection (2, 0, 0) are observed with the propagation vector along the ⟨110⟩ directions: $\mathbf{Q}^{D1} = (q, -q, 0)$ or $\mathbf{Q}^{D2} = (q, q, 0)$. Figure 2d indicates that q is not perfectly matched to the lattice, i.e., incommensurate, in GdAlSi: $q = 2/3 + \delta$ with $\delta = 0.006$.

Polarization analysis of the scattered X-rays reveals that the zero-field state of GdAlSi is the only known, undistorted helimagnetic spin texture in a magnetic Weyl semimetal[12,13]. In general, the Fourier transformed magnetic moment $\mathbf{m}(\mathbf{Q})$ is separated into three mutually orthogonal components:

$$\mathbf{m}(\mathbf{Q}) = m_c(\mathbf{Q})\mathbf{e}_c + m_{\parallel}(\mathbf{Q})\mathbf{e}_Q + m_{\perp}(\mathbf{Q})\mathbf{e}_c \times \mathbf{e}_Q, \quad (2)$$

where $\mathbf{e}_c$ and $\mathbf{e}_Q$ are unit vectors along the [001] direction of the tetragonal structure and along **Q**, respectively. In our experiment, the incident X-rays are linearly polarized with their electric field component within the scattering plane (π-plane). The scattered X-rays can have two polarization components: parallel (π') and perpendicular (σ') to the scattering plane. These two polarization

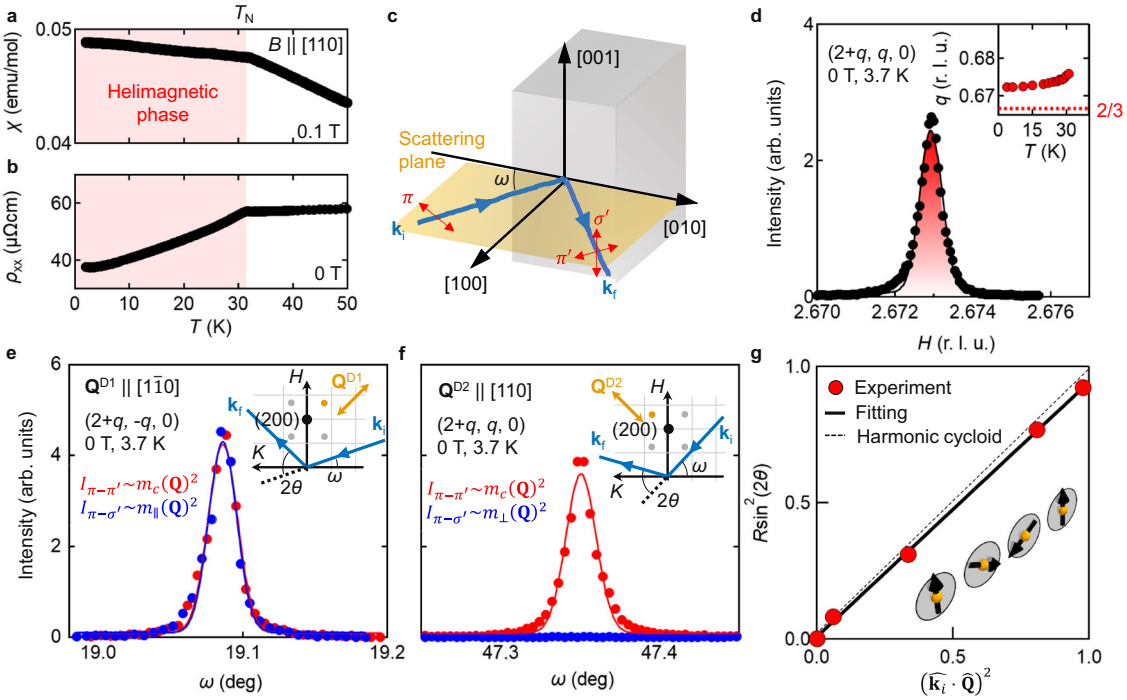

Fig. 2 | Undistorted helimagnetic ground state of GdAlSi from resonant elastic X-ray scattering (REXS). a Temperature-dependent magnetic susceptibility χ in a small magnetic field applied. The Néel point T_N is indicated. **b** Metallic, *T*-dependent resistivity ρ_{xx} with a decrease below T_N. **c** Experimental configuration of resonant elastic X-ray scattering (REXS) measurements (Methods). The scattering plane (yellow) is perpendicular to [001]. π (π', σ') represent the polarization direction of the incident (scattered) X-ray beam with wave vector $\mathbf{k}_i$ ($\mathbf{k}_f$), respectively. X-rays are incident on the sample surface at an angle ω (Methods). **d** REXS line scan profile of the (2+*q*, *q*, 0) magnetic reflection without analyzer plate, where $q = 2/3 + \delta$ and $\delta = 0.006$; Gaussian fit is shaded in red. Inset: *T*-dependence of *q* in $\mathbf{Q}_2 = (q, q, 0)$, evidencing incommensurability with the lattice. **e**, **f** Polarization analysis in REXS, assuming equal population of helimagnetic domains in zero magnetic field. **e** Rocking scan (ω) profile around (2+*q*, −*q*, 0), which is a contribution from the $\mathbf{Q}^{D1} \parallel [1\bar{1}0]$ domain. $I_{\pi-\pi'}$ and $I_{\pi-\sigma'}$ reflect $m_c(\mathbf{Q})^2$ and $m_{\parallel}(\mathbf{Q})^2$, respectively, where $m_c(\mathbf{Q})$, $m_{\parallel}(\mathbf{Q})$, and $m_{\perp}(\mathbf{Q})$ are Fourier modes of the magnetic moment along the [001] direction, along **Q**, and along the axis perpendicular to both of them, respectively (Eq. (2)). Inset: experimental setup projected onto the *HK*0 scattering plane. **f** The corresponding rocking scan of (2+*q*, *q*, 0) originating from the $\mathbf{Q}^{D2} \parallel [110]$ domain. Here, $I_{\pi-\pi'}$ and $I_{\pi-\sigma'}$ mainly reflect $m_c(\mathbf{Q})^2$ and $m_{\perp}(\mathbf{Q})^2$, respectively. **g** Undistorted helimagnetic cycloid structure with $m_{\parallel}(\mathbf{Q})/m_c(\mathbf{Q}) = 0.966(7)$ obtained by polarization analysis in REXS at various magnetic reflections. The model expectation for a harmonic cycloid is indicated by the dashed line. Inset: helimagnetic cycloidal texture.

https://doi.org/10.1038/s41467-026-69452-7

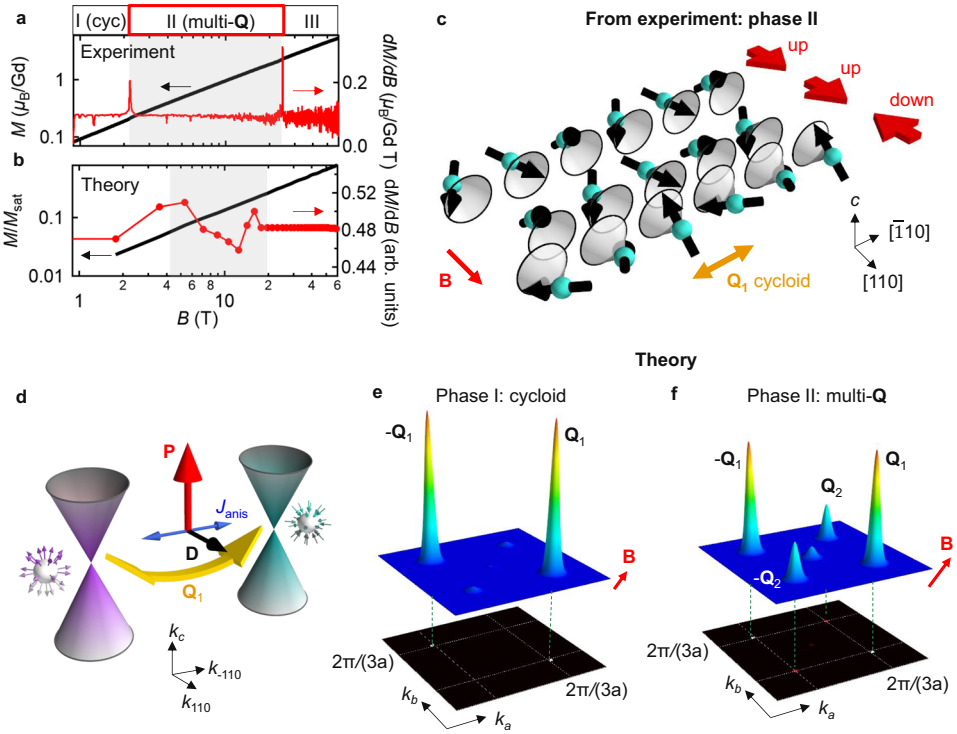

Fig. 3 | Field-induced multi-Q spin textures and magnetic model calculations for the Weyl semimetal GdAlSi. a, **b** Magnetization isotherms at $T = 4.2$ K from experiment and model calculations. The magnetic field **B** is along the [110] axis. Two B-induced transitions are visible as sharp maxima in dM/dB. **c** Multi-**Q** magnetic texture observed in phase II of GdAlSi. The structure is composed of an incommensurate, harmonic cycloid along $\mathbf{Q}_1$ and a commensurate, collinear up-up-down texture with moments parallel to **B**. See Supplementary Note S1 for detailed experiments on this structure. **d** Illustration of two Weyl cones of opposite charge and the magnetic interactions allowed for the polar (polarization **P**||[001]) crystal structure of this material: The Dzyaloshinskii-Moriya (DM) interaction **D**⊥**Q** and the anisotropic exchange interaction J_{anis}, which favor cycloidal and proper-screw habits, respectively. **e**, **f** Magnetic scattering intensity $I(\mathbf{Q})$ in the $k_c = 0$ plane calculated from Eq. (3) in the $B = 0$ ground state and in the field-induced state; the undistorted cycloid and the magnetic texture of (**c**) are well reproduced.

components are separated at the detector (Methods). In our geometry, the $\pi - \pi'$ scattered intensity always detects $m_c(\mathbf{Q})$; we further select two representative magnetic reflections for which the intensity of the $\pi - \sigma'$ channel corresponds to $m_{\parallel}(\mathbf{Q})$ and $m_{\perp}(\mathbf{Q})$ in Eq. (2), respectively. Figure 2e, f suggests that GdAlSi has $m_c(\mathbf{Q})$ and $m_{\parallel}(\mathbf{Q})$ of comparable magnitude, but not $m_{\perp}(\mathbf{Q})$: this corresponds to a harmonic helimagnetic cycloidal structure at zero magnetic field, which is further confirmed by quantitative analysis with $m_{\parallel}(\mathbf{Q})/m_c(\mathbf{Q}) = 0.966(7)$ in Fig. 2g. This incommensurate magnetic cycloid has face-centered orthorhombic symmetry (magnetic space group $Fdd2$. When approximated as a commensurate structure with $q = 2/3$, the magnetic space group is $Fd'd'2$.).

Multi-Q spin textures of GdAlSi induced by a magnetic field

We apply a magnetic field to the cycloidal helimagnetic ground state of GdAlSi (phase I), **B**||[110], and observe two field-induced transitions in Fig. 3a, b. Strictly speaking, the critical field for the transition into the field-aligned ferromagnetic state, $B_c \approx 75$ T, is beyond our experimental range. We estimate B_c by linear extrapolation of $M(B)$ to the saturation magnetization of Gd^{3+}, 7 μ_B. Using REXS with polarization analysis in an applied field of 7 T along the [110] direction, we determine the magnetic structure of phase II (Supplementary Fig. S1). As summarized by the illustration in Fig. 3c, this is a superposition of two magnetic waves, termed a multi-**Q** state: the dominant component is an incommensurate magnetic cycloid along $\mathbf{Q}_1 = (q, -q, 0)$ with $q \approx 0.673(2)$, whose spin components are in the $[1\bar{1}0]$-c plane, perpendicular to **B**. This is paired with a subdominant up-up-down pattern along the commensurate $\mathbf{Q}_2 = (2/3, 2/3, 0)$ for the spin component parallel to **B**, $\mathbf{m}_{[110]}(\mathbf{Q})$. The combination of incommensurate and commensurate modulations can be depicted as a staggered cone structure, as in Fig. 3c.

Spin model calculations and field-induced phase transition

GdAlSi's simple helimagnetic cycloidal order in zero magnetic field can be explained from a simple model of frustrated isotropic exchange interactions, as in Fig. 1c, d, when adding Dzyaloshinskii-Moriya interactions (DMI) that are allowed by the symmetry of the polar crystal structure[31]. While this real-space spin Hamiltonian provides intuitive understanding, it suffers from an inherent frustration of model parameters. Therefore, to reproduce the helimagnetic multi-**Q** textures under a magnetic field, we fix the direction and amplitude of **Q** and introduce a Fourier-space model that includes both DMI and anisotropic exchange interactions. This model is discussed in the following. Figure 3d illustrates the relative alignment of the ordering vector **Q**, the polarization **P** imposed by the $I4_1md$ crystal structure, the Dzyaloshinskii-Moriya (DM) vector **D**, and the anisotropic exchange J_{anis}. Consider the example of $\mathbf{Q}_1||[1\bar{1}0]$: Here, the relevant **D** couples the magnetization components $\mathbf{m}_{1\bar{1}0} \rightarrow \mathbf{m}_{[1\bar{1}0]}$ ($\mathbf{Q}_1$) and $m_c(\mathbf{Q}_1)$, whereas J_{anis} couples $\mathbf{m}_{[1\bar{1}0]}(\mathbf{Q}_1)$ and $m_{[1\bar{1}0]}(\mathbf{Q}_1)$.

We use an effective Fourier-space Hamiltonian on a square lattice, which includes both DMI and anisotropic exchange interactions in the matrix $\Gamma^{\alpha\beta}_{\mathbf{Q}_\nu}$[32], viz.

$$\mathcal{H} = -2\sum_{\nu,\alpha,\beta}\Gamma^{\alpha\beta}_{\mathbf{Q}_\nu} m_\alpha(\mathbf{Q}_\nu) m_\beta(\mathbf{Q}_\nu) - \sum_i \mathbf{B}\cdot\mathbf{m}(\mathbf{r}_i), \tag{3}$$

where $m_\alpha(\mathbf{Q}_\nu)$ with $\alpha = x, y, z$ and ν = a-h are Fourier components of the localized magnetic moment $\mathbf{m}(\mathbf{r}_i)$; ν = a, b are incommensurate with the lattice, ν = c, d are commensurate, and ν = e-h represent higher harmonics formed by superposition of ν = a-d (Methods). The second term represents the Zeeman energy with $\mathbf{B} = (B, B, 0)/\sqrt{2}$.

In Fig. 3e, f, we show the calculated magnetic scattering intensities, i.e., the square of the magnetic structure factor, for phases I and II. The model reproduces the cycloidal helimagnetic ground state, with two incommensurate Fourier components $\pm\mathbf{Q}_1$. Moreover, the model also features the field-induced phase II, with two strong and incommensurate reflections at $\pm\mathbf{Q}_1$ of cycloidal spin habit, combined with two weaker commensurate reflections at $\pm\mathbf{Q}_2$ with collinear spin habit (spins parallel to **B**). In other words, the calculation is well consistent with the experimental magnetic structure in zero field (Fig. 1b) and in finite magnetic field (Supplementary Fig. S1). This good alignment between theoretical and experimental results, as a function of magnetic field, supports the accuracy of our magnetic structure analysis in Figs. 2, 3. It also indicates that the Hamiltonian of Eq. (3) is suitable to describe magnetic order in GdAlSi. In Supplementary Note S5, we further truncated the Fourier-space model of Eq. (3) after a few near-neighbors and recover the intuitive real-space Hamiltonian in Fig. 1c. The present model describes effective magnetic interactions between local magnetic moments, which are implicitly mediated by conduction electrons. However, models of itinerant magnetism may provide a complementary perspective on the spin cycloid and multi-**Q** order in GdAlSi[33–35].

Discussion

Our Hamiltonian model focuses on Fourier components with characteristic propagation vectors $\mathbf{Q}_\nu$, which are well matched to the Fermi surface of GdAlSi in Fig. 1e. Here, pairs of Weyl nodes facing each other along the [110] direction are connected by **Q**, cf. Fig. 1a, and we expect a strong response of the electron gas when the helimagnetic **Q**-vector changes its direction[12]. Indeed, controlling these **Q**-domains in magnetic Weyl semimetals, by magnetic field or current, provides a valley-selective way to open a (partial) charge gap at the Weyl cones, if they have an energy-like causal connection in the folded Brillouin zone[8]. GdAlSi will serve as a prototypical material for studying the modification of Weyl nodes by a perfect helimagnetic cycloid, in contrast to the previously reported materials that exhibit a net magnetization (NdAlSi/Ge)[12,14,24,30].

Our study also emphasizes the role of symmetry-allowed Dzyaloshinskii-Moriya (DM) interactions, which favor the cycloidal spin habit, combined with anisotropic exchange, which stabilizes the multi-**Q** order in a magnetic field. As compared to previous studies[12–15,29], we here demonstrate the helimagnetic state in GdAlSi by rigorous polarization analysis; this is necessary to determine the spin rotation plane, which must form the basis for any discussion of DM or anisotropic exchange interactions. Note that the screw-type DM interaction, which has been proposed for magnetic Weyl systems[9,11], is strictly symmetry-forbidden by the polar crystal structure of *R*AlSi, *R* = rare earth (Supplementary Note S6 and Supplementary Fig. S12). However, proper-screw states can be stabilized by the presently observed anisotropic exchange interactions. Anisotropic exchange, which is known to promote complex spin textures[36], may play a role not only in NdAlSi[12,13,15] but also in the wider class of inversion breaking Weyl semimetals.

Methods

Crystal growth and characterization

Single crystals of GdAlSi were synthesized by the Al flux method. High purity chunks of Gd, Al, and Si were loaded into alumina crucibles with molar ratio Gd:Al:Si = 1: 20: 2, sealed in an evacuated quartz tube, heated to 1175 °C, held at this temperature for 12 h, cooled to 700 °C at 0. 7 °C/h, kept at 700 °C for 12 h, and centrifuged to remove residual Al flux. The samples were characterized by powder X-ray diffraction (XRD) of crushed single crystals and by Laue X-ray diffraction of single crystals.

Magnetization and electrical transport measurements

Magnetization was measured with a Magnetic Property Measurement System (MPMS, Quantum Design) and with the vibrating sample magnetometer (VSM) option of a Physical Property Measurement System (PPMS, Quantum Design). The *M*-*H* curve up to 60 T in Fig. 3a was measured in a pulsed magnetic field using an induction method with coaxial pickup coils. Electric transport measurements with rectangular shaped samples were performed using the PPMS. A standard four-probe method was applied to enable precise transport measurements irrespective of contact resistances.

Resonant elastic X-ray scattering (REXS)

REXS measurements were performed at beamline BL19LXU of SPring-8 and BL-3A of Photon Factory, KEK. The photon energy of the incident X-rays was tuned to the Gd L_2 absorption edge (~7.936 keV), corresponding to the $2p_{1/2}$ to $5d$ transition (Supplementary Figs. S13 and S14). For the zero field measurements at SPring-8, a single crystal of GdAlSi with a polished (100) surface was set in a cryostat so that the scattering plane was (*H*, *K*, 0). For the finite field measurements at KEK, we set the sample in a vertical-field superconducting magnet with a scattering plane close to (*H*, *H*, *L*), so that the magnetic field was applied almost along the [110] direction.

At both SPring-8 and KEK, the incident X-rays had linearly polarized electric field in the scattering plane (π-polarization). The (006) reflection of a pyrolytic graphite (PG) plate with $2\theta = 88.6^\circ$ was used to detect the polarization component of the scattered X-rays in the scattering plane (π') and out of the scattering plane (σ'), by rotating the PG plate around the X-ray beam. Leakage of unwanted polarization components is only 0.6 %. Inserting the analyzer plate changes the absolute scattering intensity by almost two orders of magnitude. However, in the present study we quantitatively analyze the relative strength of the π-π' and π-σ' channels. Therefore, neither the difference in absolute intensity nor the momentum-transfer dependence significantly affect our conclusions. The PG plate had a size of ~3 cm × 3 cm, sufficiently larger than the incident beam size (~1 mm × 1 mm), ensuring that the entire beam was covered and that geometrical effects are negligible. During the resonant process, the X-ray photons couple to the $5d$ conduction electrons, which in turn are coupled to the localized $4f$ magnetic moments. The resonant scattering amplitude f_{res} can be expressed as

$$f_{\mathrm{res}} = C_0 \varepsilon_{\mathrm{f}}^{*} \cdot \varepsilon_{\mathrm{i}} + iC_1(\varepsilon_{\mathrm{f}}^{*} \times \varepsilon_{\mathrm{i}}) \cdot \mathbf{m}(\mathbf{Q}) + C_2 \varepsilon_{\mathrm{f}}^{\dagger} O \varepsilon_{\mathrm{i}}, \tag{4}$$

where C_i, ε_{i}, ε_{f}, and $\mathbf{m}(\mathbf{Q})$ are constants, the polarization vectors of the incident and scattered X-rays, and the Fourier component of the magnetic moment, respectively. Among these terms, only the second term depends explicitly on $\mathbf{m}(\mathbf{Q})$, and thus encodes information about the magnetic structure. Consequently, the resonantly enhanced scattering intensity $I = f_{\mathrm{res}} \cdot f_{\mathrm{res}}^{*}$ is given as follows[37];

$$I \propto |(\varepsilon_{\mathrm{i}} \times \varepsilon_{\mathrm{f}}) \cdot \mathbf{m}(\mathbf{Q})|^2. \tag{5}$$

In our experiments, the intensity $I_{\pi-\pi'}$ for the $\pi - \pi'$ channel is proportional to $|m_{\mathrm{out}}(\mathbf{Q})|^2$ and the intensity $I_{\pi-\sigma'}$ for the $\pi - \sigma'$ channel is proportional to $(\mathbf{m}_{\mathrm{in}}(\mathbf{Q}) \cdot \mathbf{k}_{\mathrm{i}})^2$, where $\mathbf{m}_{\mathrm{in}}(\mathbf{Q})$ and $m_{\mathrm{out}}(\mathbf{Q})$ are magnetic moments in the scattering plane and perpendicular to it. In our experimental geometry, $m_{\mathrm{out}}(\mathbf{Q})$ corresponds to $m_{\mathrm{c}}(\mathbf{Q})$, and $\mathbf{m}_{\mathrm{in}}(\mathbf{Q})$ is separated into $m_{\parallel}(\mathbf{Q})$ and $m_{\perp}(\mathbf{Q})$ as described in the Main Text.

The harmonic cycloidal structure at zero field obtained in Fig. 2g is supported by the absence of higher-harmonic reflections (Supplementary Note S7 and Supplementary Figs. S5, S15) and by neutron diffraction measurements (Supplementary Note S2 and Supplementary Fig. S2).

Fourier-space model calculations

The data in Fig. 3e, f and Supplementary Fig. S16 are obtained by simulated annealing for an effective spin Hamiltonian on a two-

dimensional square lattice,

$$\mathcal{H} = -2\sum_{\nu,\alpha,\beta}\Gamma^{\alpha\beta}_{\mathbf{Q}_\nu} m_\alpha(\mathbf{Q}_\nu) m_\beta(\mathbf{Q}_\nu) - \sum_i \mathbf{B}\cdot\mathbf{m}(\mathbf{r}_i), \tag{6}$$

where $m_\alpha(\mathbf{Q}_\nu)$ with $\alpha = x, y, z$, ν = a-h are Fourier components of the localized magnetic moment $\mathbf{m}(\mathbf{r}_i)$, and $\Gamma^{\alpha\beta}_{\mathbf{Q}_\nu}$ is a matrix containing the DMI and anisotropic exchange interaction. The second term represents the Zeeman energy with $\mathbf{B} = (B, B, 0)/\sqrt{2}$. $N = 60^2$ is the total number of spins and the amplitude of each spin is fixed to unity. To obtain the low-energy spin configuration, the temperature is gradually reduced from $T = 1$ to $T = 0.001$ with a ratio $T_{n+1} = \alpha T_n$, where T_n is the nth-step temperature and α is set between 0.999990 and 0.999999. At each temperature, a local spin update is performed in real space based on the standard Metropolis algorithm. At the final temperature, 10^5–10^6 Monte Carlo sweeps are performed for the measurement.

The explicit propagation vectors in Eq. (6) are: $\mathbf{Q}_a = (q, q, 0)$, $\mathbf{Q}_b = (-q, q, 0)$, $\mathbf{Q}_c = (q', q', 0)$, $\mathbf{Q}_d = (-q', q', 0)$, $\mathbf{Q}_e = 2\mathbf{Q}_a + \mathbf{Q}_d$, $\mathbf{Q}_f = 2\mathbf{Q}_a - \mathbf{Q}_d$, $\mathbf{Q}_g = 2\mathbf{Q}_b + \mathbf{Q}_c$, and $\mathbf{Q}_h = 2\mathbf{Q}_b - \mathbf{Q}_c$ with $q = 0.35$ and $q' = 1/3$. Here, $\mathbf{Q}_a$ and $\mathbf{Q}_b$ are the incommensurate wave vectors, $\mathbf{Q}_c$ and $\mathbf{Q}_d$ are the commensurate wave vectors, and $\mathbf{Q}_e$–$\mathbf{Q}_h$ are higher harmonic wave vectors that assist the stabilization of the field-induced distorted helimagnetic state consisting of several spin density waves. To map the three-dimensional spin structures onto the two-dimensional square lattice, $q = 0.35$ and $q' = 1/3$ are incorporated, instead of the experimentally observed $q = 2/3 + \delta$ ($\delta = 0$ and 0.006).

The model parameters of the exchange matrix in Eq. (3) are set to satisfy the effective 4-fold rotational symmetry of the crystal structure of GdAlSi as follows[38]: The isotropic exchange interaction is given by $\Gamma^{xx}_a = \Gamma^{yy}_a = \Gamma^{zz}_a = \Gamma^{xx}_b = \Gamma^{yy}_b = \Gamma^{zz}_b \equiv J$, $\Gamma^{xx}_c = \Gamma^{yy}_c = \Gamma^{zz}_c = \Gamma^{xx}_d = \Gamma^{yy}_d = \Gamma^{zz}_d \equiv \alpha_1 J$, and $\Gamma^{xx}_e = \Gamma^{yy}_e = \Gamma^{zz}_e = \Gamma^{xx}_f = \Gamma^{yy}_f = \Gamma^{zz}_f = \Gamma^{xx}_g = \Gamma^{yy}_g = \Gamma^{zz}_g = \Gamma^{xx}_h = \Gamma^{yy}_h = \Gamma^{zz}_h \equiv \alpha_2 J$, the DMI is given by $\Gamma^{zx}_a = -\Gamma^{xz}_a = \Gamma^{zy}_a = -\Gamma^{yz}_a = -\Gamma^{zx}_b = \Gamma^{xz}_b = \Gamma^{zy}_b = -\Gamma^{yz}_b \equiv D$ and $\Gamma^{zx}_c = -\Gamma^{xz}_c = \Gamma^{zy}_c = -\Gamma^{yz}_c = -\Gamma^{zx}_d = \Gamma^{xz}_d = \Gamma^{zy}_d = -\Gamma^{yz}_d \equiv \alpha_1 D$, and the symmetric anisotropic exchange interaction is given by $\Gamma^{xy}_a = \Gamma^{yx}_a = -\Gamma^{xy}_b = -\Gamma^{yx}_b \equiv E$ and $\Gamma^{xy}_c = \Gamma^{yx}_c = -\Gamma^{xy}_d = -\Gamma^{yx}_d \equiv \alpha_1 E'$ with $J = 1$, $\alpha_1 = 0.98$, $\alpha_2 = 0.95$, $D = 0.01$, $E = 0.045$, and $E' = 0.05$. With these parameters, the harmonic spin cycloid at zero field and multi-**Q** order under a high magnetic field are reproduced, see also Supplementary Notes S3, S8 and Supplementary Figs. S16, S17, and S18.

Electronic structure calculations

First-principles calculations of the electronic structure were carried out using the all-electron, full-potential Korringa-Kohn-Rostoker Green's function method[39]. Relativistic spin-orbit coupling was included self-consistently, and the Gd atoms were treated with the generalized gradient approximation (GGA) exchange-correlation functional with a Hubbard U (GGA + U)[40]. U was chosen to be 6 eV. The angular momentum cutoff for the Green's function orbital expansion was set to $l_{max} = 3$, and the complex energy contour was defined using 51 integration points. To reduce computational cost, the calculations are carried out based on the primitive crystallographic unit cell, not the conventional unit cell (Supplementary Fig. S9). Self-consistent calculations for the primitive cell were performed with a **k**-mesh of 30 × 30 × 30. For Fig. 1e and Supplementary Fig. S8a, b, Fermi surface cuts were computed from the quasiparticle density of states (QDOS) in the fully polarized ferromagnetic state[41]. For the primitive helimagnetic supercell, we considered a **k**-mesh of 4 × 4 × 4 and the Gd magnetic moments were constrained to the helimagnetic configuration with propagation vector $\mathbf{Q} = (2/3, 2/3, 0)$ (Supplementary Fig. S8). Effective magnetic interactions between the Gd 4*f* magnetic atoms are computed using the infinitesimal rotation method (Supplementary Fig. S6)[31,42–44]. The Berry curvature integrated over all the occupied states in the ferromagnetic state is shown in Supplementary Fig. S7.

Second harmonic generation (SHG)

SHG measurements were performed to show inversion-symmetry breaking of bulk GdAlSi in the paramagnetic phase at room temperature. As a light source, we used a Ti:sapphire oscillator (MaiTai HP, Spectra Physics) with a pulse duration of 100 fs, repetition rate of 80 MHz, and center wavelength of 800 nm. The laser pulse is focused onto the *c*-plane surface of GdAlSi in 45-degree oblique incidence and the reflected SHG is detected by a spectrometer equipped with a liquid-nitrogen-cooled charge coupled device. Supplementary Fig. S4a, b respectively show the incident light-polarization dependence of horizontally polarized (P_{out}) and vertically polarized (S_{out}) SHG intensity at room temperature; the output polariser is fixed with polarization parallel to the [101]-axis (P_{out}) and [010] axis (S_{out}). We observed a clear polarization anisotropy of SHG in both cases, in accord with the inversion breaking crystal symmetry. In the paramagnetic phase with point group 4*mm*, the allowed terms for the horizontally polarized (P_{out}) and vertically polarized (S_{out}) SHG intensities, $I_P(\phi)$ and $I_S(\phi)$, are,

$$I_P(\phi) \propto \frac{1}{8}\left[(2a\chi_{xxz} + b\chi_{zxx} + c\chi_{zzz})\cos^2\phi + 2d\chi_{zyy}\sin^2\phi\right]^2, \tag{7}$$

$$I_S(\phi) \propto 2\left[e\chi_{yyz}\cos\phi\sin\phi\right]^2. \tag{8}$$

Here, $\chi_{ijk}(2\omega)$ and ϕ represent a tensor element of the second-order nonlinear optical susceptibility and the polarization angle for the fundamental light, respectively; a, b, c, d, and e denote prefactors including the Fresnel coefficient, beam conditions of the incident light, and so on. As shown in Supplementary Fig. S4b, c, the model well reproduces the observed anisotropy of SHG polarization, which highlights inversion breaking of the crystal, in particular the absence of a horizontal mirror plane.

Data availability

All experimental data to reproduce the figures are available on Zenodo at https://doi.org/10.5281/zenodo.18228967[45].

Code availability

The source code used to perform the calculations described in this paper is available from the corresponding authors upon request.

References

1. Armitage, N. P., Mele, E. J. & Vishwanath, A. Weyl and Dirac semimetals in three-dimensional solids. *Rev. Mod. Phys.* **90**, 015001 (2018).
2. Wang, Z. & Zhang, S.-C. Chiral anomaly, charge density waves, and axion strings from Weyl semimetals. *Phys. Rev. B* **87**, 161107 (2013).
3. Roy, B. & Sau, J. D. Magnetic catalysis and axionic charge density wave in Weyl semimetals. *Phys. Rev. B* **92**, 125141 (2015).
4. Roy, B., Goswami, P. & Juričić, V. Interacting Weyl fermions: phases, phase transitions, and global phase diagram. *Phys. Rev. B* **95**, 201102 (2017).
5. Sehayek, D., Thakurathi, M. & Burkov, A. A. Charge density waves in Weyl semimetals. *Phys. Rev. B* **102**, 115159 (2020).
6. Yi, J., Ying, X., Gioia, L. & Burkov, A. A. Topological order in interacting semimetals. *Phys. Rev. B* **107**, 115147 (2023).
7. Yi, J. & Burkov, A. Disordered Weyl semimetal as an array of coupled Hubbard chains. *Phys. Rev. B* **110**, 165114 (2025).
8. Chiu, W.-C. et al. Causal structure of interacting Weyl fermions in condensed matter systems. *Nat. Commun.* **14**, 2228 (2023).
9. Chang, H.-R., Zhou, J., Wang, S.-X., Shan, W.-Y. & Xiao, D. RKKY interaction of magnetic impurities in Dirac and Weyl semimetals. *Phys. Rev. B* **92**, 241103 (2015).

10. Hosseini, M. V. & Askari, M. Ruderman-Kittel-Kasuya-Yosida interaction in Weyl semimetals. *Phys. Rev. B* **92**, 224435 (2015).
11. Araki, Y. & Nomura, K. Spin textures and spin-wave excitations in doped Dirac-Weyl semimetals. *Phys. Rev. B* **93**, 094438 (2016).
12. Gaudet, J. et al. Weyl-mediated helical magnetism in NdAlSi. *Nat. Mater.* **20**, 1650 (2021).
13. Yao, X. et al. Large topological Hall effect and spiral magnetic order in the Weyl semimetal SmAlSi. *Phys. Rev. X* **13**, 011035 (2023).
14. Dhital, C. et al. Multi-*k* magnetic structure and large anomalous Hall effect in candidate magnetic Weyl semimetal NdAlGe. *Phys. Rev. B* **107**, 224414 (2023).
15. Lygouras, C. J. et al. Magnetic excitations and interactions in the Weyl ferrimagnet NdAlSi, arXiv. https://doi.org/10.48550/arXiv.2412.20743 (2024).
16. Roychowdhury, S. et al. Interplay between magnetism and topology: large topological Hall effect in an antiferromagnetic topological insulator, EuCuAs. *J. Am. Chem. Soc.* **145**, 12920 (2023).
17. Soh, J.-R. et al. Weyl metallic state induced by helical magnetic order. *npj Quantum Mater.* **9**, 7 (2024).
18. Nag, J. et al. GdAlSi: an antiferromagnetic topological Weyl semimetal with nonrelativistic spin splitting. *Phys. Rev. B* **110**, 224436 (2024).
19. Laha, A. et al. Electronic structure and magnetic and transport properties of antiferromagnetic Weyl semimetal GdAlSi. *Phys. Rev. B* **109**, 035120 (2024).
20. Xu, S.-Y. et al. Discovery of Lorentz-violating type II Weyl fermions in LaAlGe. *Sci. Adv.* **3**, e1603266 (2017).
21. Chang, G. et al. Magnetic and noncentrosymmetric Weyl fermion semimetals in the *R*AlGe family of compounds (*R* = rare earth). *Phys. Rev. B* **97**, 041104 (2018).
22. Suzuki, T. et al. Singular angular magnetoresistance in a magnetic nodal semimetal. *Science* **365**, 377 (2019).
23. Sanchez, D. S. et al. Observation of Weyl fermions in a magnetic non-centrosymmetric crystal. *Nat. Commun.* **11**, 3356 (2020).
24. Li, C. et al. Emergence of Weyl fermions by ferrimagnetism in a noncentrosymmetric magnetic Weyl semimetal. *Nat. Commun.* **14**, 7185 (2023).
25. Zhang, Y. et al. Kramers nodal lines and Weyl fermions in SmAlSi. *Commun. Phys.* **6**, 134 (2023).
26. Cheng, E. et al. Tunable positions of Weyl nodes via magnetism and pressure in the ferromagnetic Weyl semimetal CeAlSi. *Nat. Commun.* **15**, 1467 (2024).
27. Yang, H.-Y. et al. Transition from intrinsic to extrinsic anomalous Hall effect in the ferromagnetic Weyl semimetal $PrAlGe_{1-x}Si_x$. *Apl. Mater.* **8**, 011111 (2020).
28. Yang, H.-Y. et al. Noncollinear ferromagnetic Weyl semimetal with anisotropic anomalous Hall effect. *Phys. Rev. B* **103**, 115143 (2021).
29. Puphal, P. et al. Topological magnetic phase in the candidate Weyl semimetal CeAlGe. *Phys. Rev. Lett.* **124**, 017202 (2020).
30. Yang, H.-Y. et al. Stripe helical magnetism and two regimes of anomalous Hall effect in NdAlGe. *Phys. Rev. Mater.* **7**, 034202 (2023).
31. Bouaziz, J., Bihlmayer, G., Patrick, C. E., Staunton, J. B. & Blügel, S. Origin of incommensurate magnetic order in the *R*AlSi magnetic Weyl semimetals (*R* = Pr, Nd, Sm). *Phys. Rev. B* **109**, L201108 (2024).
32. Hayami, S. & Yambe, R. Stabilization mechanisms of magnetic skyrmion crystal and multiple-Q states based on momentum-resolved spin interactions. *Mater. Today Quant.* **3**, 100010 (2024).
33. Kawano, M. & Hotta, C. Phase diagram of the square-lattice Hubbard model with Rashba-type antisymmetric spin-orbit coupling. *Phys. Rev. B* **107**, 045123 (2023).
34. Jain, A., Goyal, G. & Singh, D. K. Weyl semimetallic state with antiferromagnetic order in the Rashba-Hubbard model. *Phys. Rev. B* **110**, 075134 (2024).
35. Sousa-Júnior, S.dA. & Mondaini, R. Weyl semimetallic, Néel, spiral, and vortex states in the Rashba-Hubbard model. *Phys. Rev. B* **111**, 075166 (2025).
36. Hirschberger, S., Hayami, M. & Tokura, Y. Nanometric skyrmion lattice from anisotropic exchange interactions in a centrosymmetric host. *N. J. Phys.* **23**, 023039 (2021).
37. Lovesey, S. W. & Collins, S. P. *X-ray Scattering and Absorption by Magnetic Materials*, Oxford series on synchrotron radiation No. 1 (Clarendon Press, Oxford University Press, 1996).
38. Yambe, R. & Hayami, S. Effective spin model in momentum space: toward a systematic understanding of multiple-Q instability by momentum-resolved anisotropic exchange interactions. *Phys. Rev. B* **106**, 174437 (2022).
39. Rüßmann, P. et al. DFT code, JuDFTteam/JuKKR: v3.6 (2022).
40. Perdew, J. P., Burke, K. & Ernzerhof, M. Generalized gradient approximation made simple. *Phys. Rev. Lett.* **77**, 3865 (1996).
41. Ebert, H., Köedderitzsch, D. & Minar, J. Calculating condensed matter properties using the KKR-Green's function method-recent developments and applications. *Rep. Prog. Phys.* **74**, 096501 (2011).
42. Liechtenstein, A. I., Katsnelson, M. I. & Gubanov, V. A. Exchange interactions and spin-wave stiffness in ferromagnetic metals. *J. Phys. F: Met. Phys.* **14**, L125 (1984).
43. Ebert, H. & Mankovsky, S. Anisotropic exchange coupling in diluted magnetic semiconductors: ab initio spin-density functional theory. *Phys. Rev. B* **79**, 045209 (2009).
44. Solovyev, I. V. Exchange interactions and magnetic force theorem. *Phys. Rev. B* **103**, 104428 (2021).
45. Nakano, R. Dataset for: Perfectly harmonic spin cycloid and multi-Q textures in the Weyl semimetal GdAlSi. *Zenodo*. https://doi.org/10.5281/zenodo.18228967 (2026).

Acknowledgements

We acknowledge fruitful discussions with Max T. Birch, Moritz M. Hirschmann, and Chris J. Lygouras. Support is acknowledged from the Japan Society for the Promotion of Science (JSPS) under Grant Nos. JP22H04463, JP23H05431, JP21K13873, JP22F22742, JP22K20348, JP23K13057, JP23H04862, JP24H01607, JP24H01604, JP21H01037, JP23H04869, JP23K13068, and JP25K17336. The work was partially supported by the Japan Science and Technology Agency via JST CREST Grant Numbers JPMJCR1874 and JPMJCR20T1 (Japan), JST FOREST Grant Numbers JPMJFR2238, JPMJFR2366, and JPMJFR212X, and JST PRESTO Grant Number JPMJPR259A. We are grateful for support by the Murata Science Foundation, Yamada Science Foundation, Hattori Hokokai Foundation, Mazda Foundation, Casio Science Promotion Foundation, Inamori Foundation, Kenjiro Takayanagi Foundation, Toray Science Foundation, the Marubun Exchange Grant, the Foundation for Promotion of Material Science and Technology of Japan (MST Foundation), the Yashima Environment Technology Foundation, ENEOS Toenegeneral Research/Development Encouragement & Scholarship Foundation, and Yazaki Memorial Foundation for Science and Technology. This work was supported by the RIKEN TRIP initiative (RIKEN Quantum, Advanced General Intelligence for Science Program, Many-Body Electron Systems). J.B. was supported by the Alexander von Humboldt Foundation through the Feodor Lynen Research Fellowship. P.R.B. acknowledges SNSF Postdoc. Mobility grant P500PT217697 for financial assistance. J.M. acknowledges funding from the Deutsche Forschungsgemeinschaft (DFG, German Research Foundation) under Project No. 547968854. M.H. is supported by JST as part of Adopting Sustainable Partnerships for Innovative Research Ecosystem (ASPIRE; Grant No. JPMJAP2426) and by the Deutsche Forschungsgemeinschaft (DFG, German Research Foundation) via Transregio TRR 360-492547816. Resonant X-ray scattering at SPring-8 was carried out under proposal number 20220083. Resonant X-ray scattering at Photon Factory (KEK) was carried out under proposal numbers 2022G551 and 2023G611. The synchrotron single-crystal X-ray experiments were performed at BL02B1 in SPring-8 with the approval of RIKEN (Proposal No. 2024B2010).

Author contributions

M.H. and Y.To. conceived the project. R.N., R.Y., A.K., and Y.Tag. grew and characterized the single crystals. R.N. and R.Y. performed all magnetic and electric measurements. R.N., R.Y., H.O., Y.Tan., and M.H. performed resonant X-ray scattering experiments at beamline BL19LXU of SPring-8. R.N., R.Y., M.G., H.S., H.N., and M.H. performed resonant X-ray scattering experiments at beamline BL-3A of Photon Factory. REXS experiments were designed and REXS data were analyzed under the guidance of T.-h.A. M.C. and J.M. performed Monte Carlo calculations of the real-space model. K.S., Y.O., and Y.Tak. performed SHG measurements. K.G. and O.F. performed neutron scattering measurements. R.N., Y.I., K.G., O.F., and M.H. analyzed the neutron scattering data. S.H. performed simulated annealing of the momentum space model. R.M., P.R.B., S.K., and Y.N. performed single-crystal X-ray diffraction measurements at SPring-8. J.B. performed and analyzed all first-principles calculations. J.B. and R.A. discussed the ab initio results. R.N., R.Y., and M.H. wrote the manuscript with help of J.B., J.M., and S.H.; all authors discussed the results and commented on the manuscript.

Competing interests

The authors declare no competing interests.

Additional information

Supplementary information The online version contains supplementary material available at https://doi.org/10.1038/s41467-026-69452-7.

Correspondence and requests for materials should be addressed to Rinsuke Yamada, Juba Bouaziz or Max Hirschberger.

Peer review information *Nature Communications* thanks Chetan Dhital and the other anonymous reviewer(s) for their contribution to the peer review of this work. A peer review file is available.